

## SELECTION OF PERSISTENT SCATTERER INTERFEROMETRIC SYNTHETIC APERTURE RADAR MASTER IMAGE CONSIDERING TEMPORAL BASELINE, SPATIAL BASELINE AND DOPPLER CENTROID FREQUENCY DIFFERENCE

Yao Lu<sup>1,2,\*</sup>, Jixian Zhang<sup>2</sup>, Xiaohua Tong<sup>1</sup>, Xiaoping Lu<sup>3</sup>, Wenli Han<sup>2</sup>, He Zhang<sup>2</sup>, Haitao Zhao<sup>2</sup>, Xiaobang Liu<sup>4</sup>

<sup>1</sup> School of Surveying and Geo-Informatics, Tongji University, Shanghai, China - 156291029@qq.com, xhtong@tongji.edu.cn

<sup>2</sup> National Quality Inspection and Testing Center For Surveying and Mapping Products, Beijing, China - zhangjx@casm.ac.cn, 88212479@qq.com, 3885987@qq.com, 85623202@qq.com

<sup>3</sup> Key Laboratory of Spatio-Temporal Information and Ecological Restoration of Mines, Ministry of Natural Resources of the People's Republic of China, Henan Polytechnic University, Jiaozuo, China - lxp@hpu.edu.cn

<sup>4</sup> School of Remote Sensing and Information Engineering, Wuhan University, Wuhan, China - liuxb555@163.com

### Commission III, WG III/3

**KEY WORDS:** PS-InSAR, Master Image, Minimum Three Baselines, Optimization Selection

#### ABSTRACT:

This paper proposed a new algorithm master Image Temporal Spatial baseline, Doppler centroid frequency difference (MITSD) to select the PS-InSAR common master image (CMI), by using the sum of temporal baselines, spatial baselines, and Doppler centroid frequency differences as a reference. The existing persistent scatterer interferometric synthetic aperture radar (PS-InSAR) common master images election method is affected by three baseline factors: temporal baseline, spatial baseline, and Doppler centroid frequency differences, then one single baseline factor in the three baselines being too large or above the baseline threshold will cause the decoherence. This method normalizes the temporal baseline, spatial baseline, and Doppler centroid frequency baseline to the same order of magnitude, and then the results of baseline optimization are summed up as the minimum coherence. Simultaneously, the algorithm in this paper sets each limit the average value of each baseline as a threshold to reduce the influence of a single baseline. The C-band Sentinel-1A single-look complex (SLC) image data (VV-polarization) in the study area was used as experimental data to compare with the MITSD, the current MSTB (minimum sum of three baselines), and CCCM (comprehensive correlation coefficient method). The results showed that (a) the baseline optimization method was more reasonable and reliable in the selection of the master image in PS-InSAR technology; and (b) in this method, the calculation steps were reduced into the calculation process, and the model was more concise than other algorithms.

#### 1. INTRODUCTION

The deformation of the Earth's surface is a process in which the ground changes relative to its original state and is often caused by compression, consolidation, and convexity of the underground loose stratum under internal or external forces. Sometimes the deformation of the Earth's surface will affect building facilities and the ground structure and cause irreversible damage and threats (Colesanti, et al., 2003, Amelung, et al., 2000). Therefore, geodetic technology plays a significant role in human production in real-time and accurate dynamic monitoring of surface deformation.

To date, numerous methods have been applied to surface-deformation monitoring. For example, traditional repetitive triangulation (Wendt, K., D. Möller, and B. Ritter, 1985) and precision leveling (Tryggvason, Eystein, 1968) provide important measurement data for surface-deformation measurements. Besides, increasingly more advanced technologies have been gradually introduced into geodetic surveys. The global navigation satellite system (GNSS) can be continuous, in real-time, and automatically monitor in the presence of limited external interference. (Dixon, Timothy H., et al, 1997, Gang, Liu, et al, 2013, Miyagi, Yousuke, et al,

2004, Engelkemeir, Richard, Shuhab D. Khan, and Kevin Burke, 2010, Bednárik, Martin, et al, 2016); digital close-range photogrammetry can obtain more deformation information based on the small-field workload (Baldi, P., et al, 2002); light detection and ranging (LiDAR) can acquire the digital surface model of the ground by scanning point clouds of the laser point, which has unique multi-angle, omnidirectional, and high-precision advantages (Muller, Jordan R., and David J. Harding, 2007, Bawden, G. W., et al, 2005, Hu, Hui, et al, 2015). However, the aforementioned methods consume a significant amount of manpower and are economically costly. In the 1990s, the main idea of the interferometric synthetic aperture radar (InSAR) was to use the phase difference of the two images to obtain a digital elevation model (DEM), which had the advantages of high resolution, wide-coverage, and high-precision measurement in the regional surface deformation monitoring (Ferretti, Alessandro, Claudio Prati, and Fabio Rocca, 2000), and was increasingly being applied to relevant monitoring studies (Wright, Tim J., Barry E. Parsons, and Zhong Lu, 2004, Lohman, Rowena B., and Mark Simons, 2005, Lu, Zhong, et al, 2010). Limited by the precision of synthetic aperture radar interferometry, scholars have introduced an external DEM or orbital differential to achieve

\* Corresponding author.

E-mail addresses: 156291029@qq.com (Yao Lu)

relative accuracy, which was called differential interferometric synthetic aperture radar (D-InSAR). Nonetheless, D-InSAR was also susceptible to Spatio-temporal decoherence, atmospheric influences, etc (Zebker, Howard A., and John Villasenor, 1992). To eliminate these effects, Ferretti proposed persistent scatterer interferometric synthetic aperture radar (PS-InSAR) based on permanent scatterers in 2000 (Ferretti, Alessandro, Claudio Prati, and Fabio Rocca, 2000), aiming to select permanent scattering features with stable time-scattering characteristics and strong echo signals to accurately reflect the relative displacement of the monitored area.

In recent years, many scholars have applied PS-InSAR technology to the field of surface-deformation monitoring, such as land subsidence, mining subsidence, landslide, and glacier movement, and have achieved remarkable research results (Sousa, Joaquim J., et al, 2010, Funning, Gareth J., et al, 2007, Greif, Vladimir, and Jan Vlcko, 2012, Peyret, M., et al, 2011, Perrone, G., et al, 2013). When PS-InSAR technology is used to monitor surface deformation, CMI selection is the most significant step for differential interference. At present, the selection of the best CMI usually takes into account the three factors of time baseline, spatial baseline, and Doppler center-frequency baseline. How to determine the relationship between these three factors ( $\alpha$ ,  $\beta$ ,  $\theta$ ) has become one of the main hotspots of related studies (Ferretti, A., C. Prati, and F. Rocca, 2001, Kampes, Bert, and N. Adam, 2003, Zhang, Hua, et al, 2005).

Liu, X., et al. (2018a) based on the combination of correlation coefficient algorithm and three baselines minimum sum algorithm, the best common master image is obtained by combining the time baseline, effective spatial baseline, and Doppler center-frequency difference of image pairs. Liu, X., et al. (2018b) proposed an error analysis method to calculate the difference evaluation tolerance and total error between the spatial-temporal baseline and Doppler centroid frequency and weighted the interferogram sequence under the condition of removing gross error to obtain the weighted and maximum optimal common master image. However, there are problems in the current studies when considering the effects of the time, space, and Doppler centroid-frequency baselines. The most serious problem is that one single baseline factor is too large among the three baselines, and the other two baselines may be ignored due to their small proportion, which causes the incoherence of a certain baseline, thus affecting the accuracy of the result. At the same time, the process of calculating the baseline error increases the complexity of the master image selection process.

Given the shortcomings of the above methods, this paper aims to improve the PS-InSAR master image three baseline and minimum selection methods for optimization. The basic idea is to sum the baselines for each image as the master image, and the larger the value, the greater the coherence. Also, the image with the largest optimization result is used as the master image. Therefore, the improved master image selection method can be discussed utilizing this new method.

## 2. MITSD METHOD

The selection of the CMI must take into account the distribution of all combinations of the time, spatial, and Doppler centroid-frequency baselines, and select the best image as the shared master image. The CCCM and the MSTB method are currently widely used as master image extraction methods with which the extent to which the spatial, temporal,

and Doppler centroid-frequency baselines affect image correlation is analyzed.

The spatial baseline correlation ( $\gamma_B$ ) is caused by the difference in the radar angles of the two observations. The longer the baseline, the lower the coherence. When the baseline exceeds the critical range, the images are irrelevant:

$$\gamma_B = \begin{cases} 1 - \frac{B_{im}}{B_\perp^c}, & B_{im} \leq B_\perp^c \\ 0, & B_{im} > B_\perp^c \end{cases} \quad (1)$$

Temporal baseline correlation ( $\gamma_T$ ) is mainly caused by changes in surface scattering characteristics during imaging, such as vegetation changes and rainfall; the longer the imaging time interval, the more seriously the time is out of coherence:

$$\gamma_T = \begin{cases} 1 - \frac{T_{im}}{T^c}, & T_{im} \leq T^c \\ 0, & T_{im} > T^c \end{cases} \quad (2)$$

The Doppler centroid-frequency baseline correlation ( $\gamma_F$ ) is caused by Doppler centroid misalignment during imaging. The larger the Doppler centroid-frequency baseline, the lower the coherence of the image:

$$\gamma_F = \begin{cases} 1 - \frac{F_{im}}{F_{DC}^c}, & F_{im} \leq F_{DC}^c \\ 0, & F_{im} > F_{DC}^c \end{cases} \quad (3)$$

The CCCM method takes into account the different degrees of influence of various factors on the overall correlation, while, regarding the time, spatial, and Doppler centroid-frequency baselines, the functional model can be explained as

$$\gamma^m = \frac{1}{N+1} \sum_{i=1}^{N+1} \left[ \left\{ 1 - f \left( \frac{|T_{im}|}{T^c} \right) \right\}^\alpha \cdot \left\{ 1 - f \left( \frac{|B_{im}|}{B_\perp^c} \right) \right\}^\beta \cdot \left\{ 1 - f \left( \frac{|F_{im}|}{F_{DC}^c} \right) \right\}^\theta \right], \quad (4)$$

where  $\gamma^m$  is the comprehensive correlation coefficient;  $T_{im}$ ,  $B_{im}$ ,  $F_{im}$  are the temporal baseline, spatial baseline, and Doppler centroid-frequency baseline of the interference pair formed between the  $i$ th auxiliary image and the master image numbered  $m$ , respectively;  $T^c$ ,  $B_\perp^c$ ,  $F_{DC}^c$  are the critical conditions corresponding to  $T_{im}$ ,  $B_{im}$ ,  $F_{im}$ , respectively, and  $\alpha$ ,  $\beta$ ,  $\theta$  are the corresponding exponential factors. By calculating  $\gamma^m$  different factors such as (1,1,1), (1,2,1), and (2,1,1).  $\gamma^m$  is then the indicator used to select CMI. However, this calculation process must measure different combination factors to determine the weight ratio of each factor, and therefore, the number of calculations increases.

The MSTB method proposes that the sum of the three baseline absolute values should be the minimum based on the importance of interference baselines for time, spatial, and Doppler centroid-frequency baselines:

$$sumB = \sum_{i=1}^N (|B_T^i| + |B_B^i| + |B_{F_{DC}}^i|) = \min \quad (5)$$

where  $N$  is the number of interferograms; and  $B_T^i, B_B^i, B_{F_{DC}}^i (i=1,2,\dots,N)$  are the time, spatial, and Doppler centroid-frequency baselines, respectively, for the  $i$ th interferogram. Although the method uses the sum of the three baseline absolute values as an indicator to measure image coherence, it is difficult to avoid the problem that the proportion of a single baseline factor in the three baselines is too great.

To reduce the impact of the three baseline weights on the master image selection, a primary image selection method for baseline optimization based on the MSTB method is proposed in this paper. This method normalizes the temporal, spatial, and Doppler centroid-frequency baselines to the same order of magnitude and then sums them. The calculation process is as follows.

Let the  $i$ th image be the CMI, and obtain the sum of the absolute values of the temporal, spatial, and Doppler centroid-frequency baselines in the interferogram formed by the image and other images:

$$\begin{aligned} S(i_T) &= \sum_{i=1}^N |B_T^{ik}| \\ S(i_B) &= \sum_{i=1}^N |B_B^{ik}| \\ S(i_{F_{DC}}) &= \sum_{i=1}^N |B_{F_{DC}}^{ik}| \end{aligned} \quad (6)$$

where  $N$  is the number of interferograms;  $B_T^{ik}, B_B^{ik}, B_{F_{DC}}^{ik} (i=1,2,\dots,N)$  represent the temporal, spatial, and Doppler centroid-frequency baselines, respectively, between the  $i$ th master image and  $k$ th image; and  $S(i_T), S(i_B), S(i_{F_{DC}})$  represent the sum of the absolute values of the temporal, spatial, and Doppler centroid-frequency baselines for the  $i$ th master image, respectively.

Next, find the sum of absolute values of the temporal, spatial, and Doppler centroid-frequency baselines for the  $N$  pairs of interference images and then average them:

$$\begin{aligned} \bar{T} &= \frac{\sum_{i=1}^N S(i_T)}{N} \\ \bar{B} &= \frac{\sum_{i=1}^N S(i_B)}{N} \\ \bar{F}_{DC} &= \frac{\sum_{i=1}^N S(i_{F_{DC}})}{N}, \end{aligned} \quad (7)$$

where  $\bar{T}, \bar{B}, \bar{F}_{DC} (i=1,2,\dots,N)$  are the average values.

The temporal baseline of the experimental data accounts for more than 50% of the sum of the three baselines. To avoid excessive weight and weaken the influence of the other two baselines on coherence, it is necessary to optimize the temporal baseline. Timebase optimization requires the calculation of the root-mean-square error (RMSE) in the temporal baseline and of the difference between the temporal baseline and average

value and construction of a function between the RMSE and difference value:

$$\Delta T = \sqrt{\frac{\sqrt{[(S(i_T) - \bar{T})^2]} }{N-1}}, \quad (8)$$

$$f(T) \begin{cases} 1, S(i_T) - \bar{T} \leq \Delta T \\ 0, S(i_T) - \bar{T} > \Delta T \end{cases}, \quad (9)$$

$$E(i_T) = f(S(i_T), \bar{T}) = f(T)(1 - \frac{S(i_T)}{\bar{T}}) \quad (10)$$

The average value obtained by Eq. (7) is used as the baseline optimization parameter for the spatial and Doppler centroid-frequency baselines. The optimization results of both parameters are then calculated, which are expressed as

$$E(i_B) = f(S(i_B), \bar{B}) \begin{cases} 1 - \frac{S(i_B)}{\bar{B}}, (S(i_B) \leq \bar{B}) \\ 0, (S(i_B) > \bar{B}) \end{cases}, \quad (11)$$

$$E(i_{F_{DC}}) = f(S(i_{F_{DC}}), \bar{F}_{DC}) \begin{cases} 1 - \frac{S(i_{F_{DC}})}{\bar{F}_{DC}}, (S(i_{F_{DC}}) \leq \bar{F}_{DC}) \\ 0, (S(i_{F_{DC}}) > \bar{F}_{DC}) \end{cases}, \quad (12)$$

In Eqs. (10)–(12),  $E(i_T), E(i_B), E(i_{F_{DC}})$  are the optimization results of the temporal, spatial, and Doppler centroid-frequency baselines of the interferogram between the  $i$ th mean image and the other images.

The master image selected by the proposed method makes the three baseline combinations optimal. The sum of the three baseline optimization values is the maximum, which means the interferogram of the  $i$ th image master has the best coherence:

$$E(i) = f(T) \left[ \sum_{i=1}^N (E(i_T) + E(i_B) + E(i_{F_{DC}})) \right] = \max \quad (13)$$

where  $N$  is the number of interferograms, and  $E(i)$  represents the sum of baseline optimization results for the  $i$ th master image. When  $f(T)=1$ , the optimization of the temporal baseline is effective; when  $f(T)=0$ , the opposite is true, indicating that the weight of the temporal baseline is too great. Therefore, the temporal baseline should be eliminated, and then, setting the three baseline optimization results as 0, this image will not participate in the selection of the master image. In the MITSD method, the baseline weight and the optimization results have an inverse relationship, which means the smaller the three baselines, the larger the optimization result value, and the greater the coherence of the master image with other images. Meanwhile, according to the characteristics of each baseline in the calculation process, the average value of each baseline [the calculation result of Eq. (7)] is used as the threshold value of the baseline parameter to eliminate the larger baseline image, reduce the number of baseline calculations when selecting

images, and eliminate the influence of a single baseline on master image selection.

### 3. EXPERIMENTAL RESULTS AND DISCUSSIONS

To verify the applicability of the MITSD method proposed in this paper, the main coal-producing areas in China are selected as the research areas. MSTB method, CCCM method, and MITSD method proposed in this paper are used to select the PS-InSAR master image respectively, and the results of the three methods are compared and analyzed.

In this section, C-band Sentinel-1A single-look complex (SLC) image data (VV polarization mode) of 21 scenes in China, were selected for testing. Figure 1 shows a cropped image of the experimental area, which measures 35 km<sup>2</sup>. The external DEM uses SRTM (Shuttle Radar Topography Mission) data at a 90-m resolution.

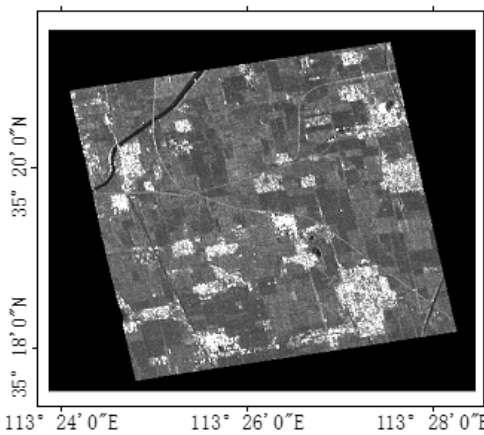


Figure 1. Experimental area SAR intensity map

The MSTB, CCCM, and MITSD methods were used to calculate the relevant data of the  $i$ th master image. Taking the maximum value of the baseline as the corresponding critical value when calculating the correlation coefficient by the CCCM algorithm, the results are shown in Tables 1 and 2.

| Image no. | Imaging date | Optimization results | SumB     |
|-----------|--------------|----------------------|----------|
| 1         | 2015-06-17   | 0                    | 5352.286 |
| 2         | 2015-06-29   | 0                    | 4905.283 |
| 3         | 2015-07-11   | 0                    | 4183.789 |
| 4         | 2015-07-23   | 0                    | 4613.612 |
| 5         | 2015-08-16   | 0.514                | 3560.650 |
| 6         | 2015-08-28   | 0.600                | 3412.385 |
| 7         | 2015-09-09   | 0.551                | 3324.120 |
| 8         | 2015-09-21   | 0                    | 3706.962 |
| 9         | 2015-10-03   | 0.564                | 3401.817 |
| 10        | 2015-10-15   | 0.633                | 3115.635 |
| 11        | 2015-10-27   | 0.567                | 4407.794 |
| 12        | 2015-11-20   | 0                    | 3177.009 |
| 13        | 2015-12-02   | 0.734                | 3124.956 |
| 14        | 2015-12-14   | 0                    | 3203.472 |
| 15        | 2015-12-26   | 0                    | 3856.030 |
| 16        | 2016-01-07   | 0                    | 4494.436 |
| 17        | 2016-03-07   | 0                    | 4016.579 |
| 18        | 2016-03-31   | 0                    | 4540.474 |
| 19        | 2016-04-12   | 0                    | 5042.374 |
| 20        | 2016-05-06   | 0                    | 4896.797 |
| 21        | 2016-05-30   | 0                    | 5418.223 |

Table 1. Comparison of Experimental Results

In Table 1, if the baseline optimization result is 0, when the baseline is optimized, a certain baseline value of the image is larger than the average value and does not participate in the selection of the master image. The minimum value (red highlighted) of the MSTB method appears at the image numbered 10, indicating that the method uses image No. 10 as the CMI. The maximum value (green highlighted) of the baseline optimization method results in image No. 13, indicating that the method uses image No. 13 as the CMI.

| Image | (111) | (121) | (112) | (122) | (211) | (221) | (212) |
|-------|-------|-------|-------|-------|-------|-------|-------|
| 1     | 0.000 | 0.000 | 0.000 | 0.000 | 0.000 | 0.000 | 0.000 |
| 2     | 0.034 | 0.010 | 0.013 | 0.004 | 0.010 | 0.003 | 0.004 |
| 3     | 0.041 | 0.021 | 0.009 | 0.005 | 0.014 | 0.007 | 0.003 |
| 4     | 0.055 | 0.012 | 0.036 | 0.008 | 0.021 | 0.005 | 0.014 |
| 5     | 0.153 | 0.079 | 0.098 | 0.051 | 0.070 | 0.036 | 0.045 |
| 6     | 0.168 | 0.088 | 0.109 | 0.057 | 0.082 | 0.043 | 0.054 |
| 7     | 0.164 | 0.086 | 0.100 | 0.052 | 0.085 | 0.044 | 0.052 |
| 8     | 0.076 | 0.028 | 0.030 | 0.011 | 0.041 | 0.015 | 0.016 |
| 9     | 0.156 | 0.066 | 0.104 | 0.044 | 0.086 | 0.037 | 0.058 |
| 10    | 0.180 | 0.096 | 0.109 | 0.058 | 0.101 | 0.054 | 0.061 |
| 11    | 0.000 | 0.000 | 0.000 | 0.000 | 0.000 | 0.000 | 0.000 |
| 12    | 0.147 | 0.078 | 0.073 | 0.039 | 0.082 | 0.043 | 0.041 |
| 13    | 0.195 | 0.107 | 0.127 | 0.070 | 0.107 | 0.059 | 0.070 |
| 14    | 0.135 | 0.076 | 0.060 | 0.034 | 0.072 | 0.041 | 0.032 |
| 15    | 0.095 | 0.030 | 0.056 | 0.018 | 0.049 | 0.015 | 0.028 |
| 16    | 0.021 | 0.003 | 0.006 | 0.001 | 0.010 | 0.001 | 0.003 |
| 17    | 0.111 | 0.062 | 0.067 | 0.038 | 0.036 | 0.020 | 0.022 |
| 18    | 0.076 | 0.036 | 0.049 | 0.023 | 0.019 | 0.009 | 0.012 |
| 19    | 0.044 | 0.015 | 0.027 | 0.009 | 0.009 | 0.003 | 0.006 |
| 20    | 0.037 | 0.021 | 0.022 | 0.013 | 0.004 | 0.002 | 0.002 |
| 21    | 0.000 | 0.000 | 0.000 | 0.000 | 0.000 | 0.000 | 0.000 |

Table 2. Calculation of Comprehensive Correlation Coefficient Results for Different Combination Factors ( $\alpha, \beta, \theta$ )

Table 2 shows the results of the CCCM method in the case of selecting different combination factors. The different combination factors obtain the maximum value in the 2015-12-02 image, i.e., image No. 13 (red highlighted), which indicates that the method selects the 2015-12-02 image as the master image. It can be seen from Table 2 that the correlation coefficient obtained by selecting different combination factors shows a certain similarity, which indicates that different combination factors have little impact on the master image selection. Thus,  $(\alpha, \beta, \theta) = (1, 1, 1)$  can be set to select the correlation coefficient of the master image for the master image selection. According to the calculation results in Tables 1 and 2, the corresponding curve is drawn as in Fig. 2. (The X-axis represents the image sequence numbers arranged in chronological order. The Y-axis represents the results of three methods. The baseline optimization result is expanded 10,000 times, and the CCCM result (1,1,1) is expanded by 20,000 times.)

The 10th and 13th scene images were used as the master images separately, and for the statistics of the time-space baseline of the other auxiliary images and the maximum, mean, standard deviation, optimized value, and comprehensive correlation coefficient of the baseline of the Doppler centroid frequency, the results are shown in Table 3.

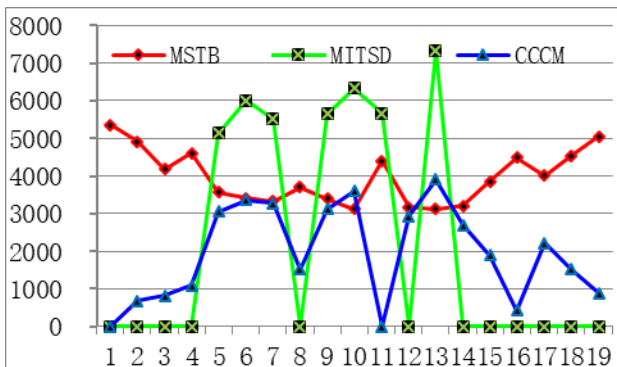
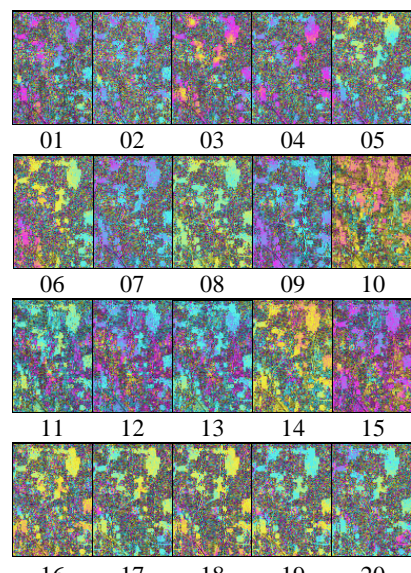


Figure 2 Experimental area results curve

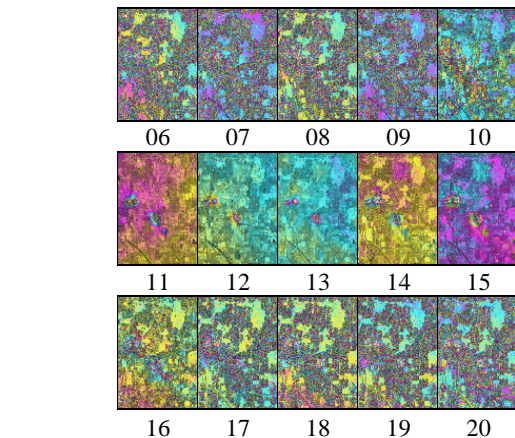
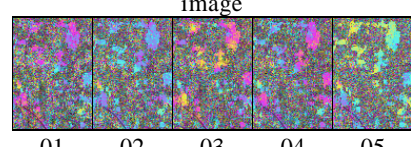
| No | Date | Base line | Max    | Average | Standard deviation | Optimization value | CCCM  |
|----|------|-----------|--------|---------|--------------------|--------------------|-------|
| 10 | 201  | T         | 228    | 86.86   | 65.72              | 0.631              | 0.18  |
|    | 5-   | B         | 120.88 | 55.35   | 38.22              |                    |       |
|    | 10-  | D         | 22.99  | 6.60    | 6.36               |                    |       |
| 13 | 201  | T         | 180    | 89.14   | 56.61              | 0.734              | 0.195 |
|    | 512  | B         | 138.46 | 53.37   | 35.81              |                    |       |
|    | 02   | D         | 16.67  | 5.85    | 4.29               |                    |       |

Table 3. Baseline values of images numbered 10 and 13

It can be seen from Table 3 that the differences between the maximum, average, and standard deviation of the spatial and Doppler centroid-frequency baselines of the two scene images are extraordinarily small. The temporal baseline standard deviation of the 13th image is smaller than that of the 10th image, and the optimization result and comprehensive correlation coefficient value are larger than the corresponding values of the 10th image. This fully proves that the interference effect of the 13th image as the master image is better than that of the 10th image.



(a) Interferogram of the 10th scene image as the master image



(b) Interferogram of the 13th scene image as the master image

Figure 3. Interferograms of 10th and 13th scene images as the master image

Figure 3(a) and (b) show interference diagrams of the images numbered 10th and 13th as the master images, respectively. The interference fringes in Fig. 3(b) are more obvious than in Fig. 3(a). In the 11th to 15th interferograms, Fig. 3(b) shows the deformation region more clearly, in which the overall interference effect is more obvious than that in Fig. 3(a). Figure 4(a) and (b) show the deformation area distribution diagrams of the 10th and 13th images, respectively. The three red circles in Fig. 4(a) are the locations of the ground-level measurement points and the red frame in Fig. 4(b) is the mining area. There are fewer buildings in the area, and PS (Persistent Scatterer) points are mostly distributed along the boundaries of the mining area. The study uses the MITSD method proposed in this paper to select the master image, focusing on the research area for deformation analysis. In this study, the PS point is selected by the coherence coefficient threshold method, in which the 20153652 image obtains 25365 PS points as the master image and 22642 PS points for the 20151015 master image.



(a) Deformation image of the 10th scene image as the master image



(b) Deformation image of the 13th scene image as the master image

Figure 4. PS-InSAR deformation area distribution map

To further analyze and verify the accuracy of the different master image selection methods, the PS points nearest the one-, two-, and three-level monitoring points in the study area are selected for timing analysis. Figure 5(a), (c), and (e) show the PS point deformation results of the 20151202 master image and Fig. 5(b), (d), and (f) show the PS point deformation results of the 20151015 master image. Compared with the leveling data, it can be found that the deformation result of the 20151202 master image is closer to the leveling result. Although the 20151015 master image obtains a more accurate distribution of deformation regions, the difference between the shape variables and leveling results is still large. The comparison between the PS points of the different master images and the ground measurements is shown in Table 4.

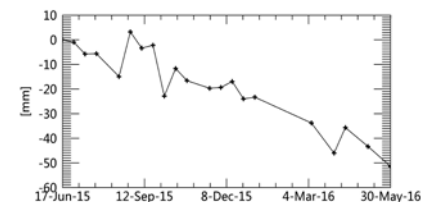
In table 4, ground measurements represent the deformation of the three measured points in the time range of 20150731–20160729, mainly resulting in settlement deformation. Difference(20151202) means that the type variable of the corresponding region is obtained by PS-InSAR with the 20151202 image (13 in Table 1) as the master image. Difference(20151015) means that the deformation of the corresponding region is obtained by PS-InSAR with the 20151015 image (10 in Table 1) as the master image. It can be seen that the deformation results obtained in 201512 phase as the master image are -51 in region 1, -21 in region 2 and -77 in region 3, which are different from the measured results by 0.8, 6.9 and 8.6 respectively. As the master image, the deformation results obtained in 201512 are 31.2, 8.1, and 24.4 different from the measured results in regions 1, 2, and 3. It can be concluded that the master image selected by this method is closer to the measured value.

Based on the above analysis, a decoherent selection model is constructed by optimizing the three master factors. Finally, the influence of the time-space and Doppler centroid-frequency baselines on image coherence was measured, which makes the method more reasonable and effective.

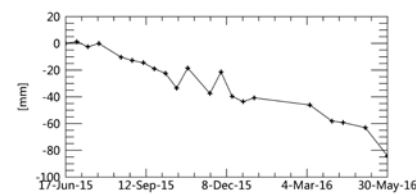
| Area | ground measurements (mm)<br>(2015-07-31~2016-07-29) | Difference<br>(2015-12-02) | Difference<br>(2015-10-15) |
|------|---|----------------------------|----------------------------|
| 1    | -51.8   | -51/0.8                    | -85/31.2                   |
| 2    | -27.9   | -21/6.9                    | -36/8.1                    |
| 3    | -68.4   | -77/8.6                    | -44/24.4                   |

Table 4. Comparison of accuracy between PS-InSAR and level monitoring results

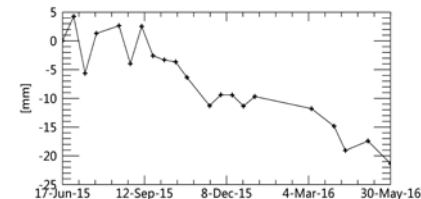
According to Fig. 5(a), (c), and (e), regions 1, 2, and 3 incurred large surface subsidence during the study time (June 2015 to May 2016), and the settlement amount was 20–70 mm; by analyzing the change process of the PS points in the three deformation regions, it was found that the subsidence of the three regions has continuity in time. The main factors causing land subsidence include urban building loads, underground minerals, and groundwater exploitation. Underground coal mining has been carried out in the study area, and the spatial location of the surface subsidence area coincides with the distribution of the coal-mining area, indicating that the coal-mining activity in the area is one of the factors leading to land subsidence.



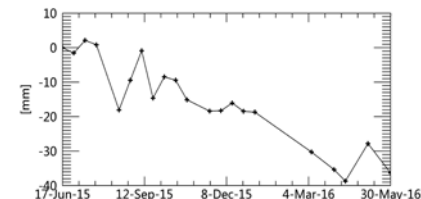
(a) Area 1 20151202 PS point deformation rate diagram



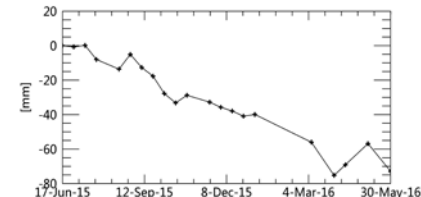
(b) Area 1 20151015 PS point deformation rate diagram



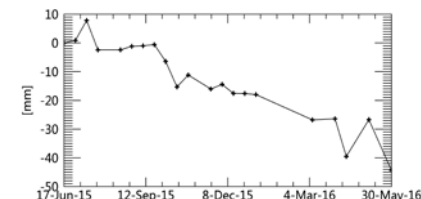
(c) Area 2 201512025 PS point deformation rate diagram



(d) Area 2 20151015 PS point deformation rate diagram



(e) Area 3 20151202 PS point deformation rate diagram



(f) Area 3 20151015 PS point deformation rate diagram

Figure 5. PS point deformation rate comparison

#### 4. CONCLUSIONS

Aiming at the shortcomings of existing CMI selection methods, in this paper, a baseline optimized master image extraction method MITSD (master Image Temporal Spatial baseline, Doppler centroid frequency difference) is proposed. This

method can effectively avoid a single baseline weight being too large and reduce the possibility of decoherence due to poor selection of the master image; by a comparative analysis of the deformation results obtained from different master images and the level data, the following conclusions were drawn.

(1) The data indicators of the MITSD method selection result are better than the MSTB method, and the deformation result is more accurate than that of the MSTB method.

(2) The MITSD method has good consistency with the CCCM. However, the MITSD method is more convenient in terms of the calculation process. There is no need to artificially set the threshold or introduce other parameters, and the algorithm model is more concise.

The research results show that the baseline optimization method is more reasonable and reliable in terms of the selection of the master image in PS-InSAR technology.

## ACKNOWLEDGEMENTS

This study was supported by NSFC (41671440), and 2016 National Key Research and Development Plan of China (2016YFC0803103).

## REFERENCES

- Amelung, F., Jónsson, S., Zebker, H., & Segall, P., 2000. Widespread uplift and ‘trapdoor’ faulting on Galapagos volcanoes observed with radar interferometry. *Nature*, 407(6807), 993.
- Baldi, P., Casula, G., Fabris, M., Ghirotti, M., Mora, P., & Pesci, A., 2002. Digital Photogrammetry and GPS Techniques For Monitoring Landslide Surface Deformation. In EGS General Assembly Conference Abstracts (Vol. 27).
- Bawden, G. W., Schmitz, S., Howle, J. F., Lacznak, R. J., Bowers, J., Osterhuber, R., & Irvine, P., 2005. Four-dimensional surface deformation analysis, snow volume calculation, and fault mapping with ground based tripod LiDAR. In AGU Fall Meeting Abstracts.
- Bednárik, M., Papčo, J., Pohánka, V., Bezák, V., Kohút, I., & Brimich, L., 2016. Surface strain rate colour map of the Tatra Mountains region (Slovakia) based on GNSS data. *Geologica Carpathica*, 67(6), 509-524.
- Colesanti, C., Ferretti, A., Novali, F., Prati, C., & Rocca, F., 2003. SAR monitoring of progressive and seasonal ground deformation using the permanent scatterers technique. *IEEE Transactions on Geoscience and Remote Sensing*, 41(7), 1685-1701.
- Dixon, T. H., Mao, A., Bursik, M., Heflin, M., Langbein, J., Stein, R., & Webb, F., 1997. Continuous monitoring of surface deformation at Long Valley Caldera, California, with GPS. *Journal of Geophysical Research: Solid Earth*, 102(B6), 12017-12034.
- Engelkemeir, R., Khan, S. D., & Burke, K., 2010. Surface deformation in Houston, Texas using GPS. *Tectonophysics*, 490(1-2), 47-54.
- Ferretti, A., Prati, C., & Rocca, F., 2001. Permanent scatterers in SAR interferometry. *IEEE Transactions on geoscience and remote sensing*, 39(1), 8-20.
- Ferretti, A., Prati, C., & Rocca, F., 2000. Nonlinear subsidence rate estimation using permanent scatterers in differential SAR interferometry. *IEEE Transactions on geoscience and remote sensing*, 38(5), 2202-2212.
- Ferretti, A., Prati, C., & Rocca, F., 2000. Nonlinear subsidence rate estimation using permanent scatterers in differential SAR interferometry. *IEEE Transactions on geoscience and remote sensing*, 38(5), 2202-2212.
- Funning, G. J., Bürgmann, R., Ferretti, A., Novali, F., & Fumagalli, A., 2007. Creep on the Rodgers Creek fault, northern San Francisco Bay area from a 10 year PS- InSAR dataset. *Geophysical Research Letters*, 34(19).
- Gang, L., Bin, Z., Rui, Z., Yong, H., Jun, W., Zhaosheng, N., ... & Kai, T., 2013. Near-field surface deformation during the April 20, 2013, Ms7. 0 Lushan earthquake measured by 1-Hz GNSS. *Geodesy and Geodynamics*, 4(2), 1-5.
- Greif, V., & Vlcko, J., 2012. Monitoring of post-failure landslide deformation by the PS-InSAR technique at Lubietova in Central Slovakia. *Environmental Earth Sciences*, 66(6), 1585-1595.
- Hu, H., Fernandez-Stegger, T. M., Dong, M., & Azzam, R., 2015. Deformation Monitoring and Recognition of Surface Mine Slope Using LiDAR. In *Engineering Geology for Society and Territory-Volume 2* (pp. 451-454). Springer, Cham.
- Kampes, B. M., & Adam, N., 2003. Velocity field retrieval from long term coherent points in radar interferometric stacks. In *IGARSS 2003. 2003 IEEE International Geoscience and Remote Sensing Symposium. Proceedings* (IEEE Cat. No. 03CH37477) (Vol. 2, pp. 941-943). IEEE.
- Liu, X., et al. (2018) a. "Optimized Method for Selecting Common Master Image in PS-DINSAR." *journal of Engineering Science and Technology Review* 11(1): 208-215.
- Liu, X., et al. (2018b). "Optimized Method for Selecting the Common Master Image in PS-InSAR Based on Error Analysis." *journal of Engineering Science and Technology Review* 11(2): 63-71.
- Lohman, R. B., & Simons, M., 2005. Some thoughts on the use of InSAR data to constrain models of surface deformation: Noise structure and data downsampling. *Geochemistry, Geophysics, Geosystems*, 6(1).
- Lu, Z., Dzurisin, D., Biggs, J., Wicks Jr, C., & McNutt, S., 2010. Ground surface deformation patterns, magma supply, and magma storage at Okmok volcano, Alaska, from InSAR analysis: 1. Intereruption deformation, 1997–2008. *Journal of Geophysical Research: Solid Earth*, 115(B5).
- Miyagi, Y., Freymueller, J. T., Kimata, F., Sato, T., & Mann, D., 2004. Surface deformation caused by shallow magmatic activity at Okmok volcano, Alaska, detected by GPS campaigns 2000-2002. *Earth, planets and space*, 56(10), e29-e32.

Muller, J. R., & Harding, D. J., 2007. Using LIDAR surface deformation mapping to constrain earthquake magnitudes on the Seattle fault in Washington State, USA. In 2007 Urban Remote Sensing Joint Event (pp. 1-7). IEEE.

Perrone, G., Morelli, M., Piana, F., Fioraso, G., Nicolò, G., Mallen, L., ... & Tallone, S., 2013. Current tectonic activity and differential uplift along the Cottian Alps/Po Plain boundary (NW Italy) as derived by PS-InSAR data. *Journal of Geodynamics*, 66, 65-78.

Peyret, M., Dominguez, S., Cattin, R., Champenois, J., Leroy, M., & Zajac, A., 2011. Present - day interseismic surface deformation along the Longitudinal Valley, eastern Taiwan, from a PS - InSAR analysis of the ERS satellite archives. *Journal of Geophysical Research: Solid Earth*, 116(B3).

Sousa, J. J., Ruiz, A. M., Hanssen, R. F., Bastos, L., Gil, A. J., Galindo-Zaldívar, J., & de Galdeano, C. S., 2010. PS-InSAR processing methodologies in the detection of field surface deformation—Study of the Granada basin (Central Betic Cordilleras, southern Spain). *Journal of Geodynamics*, 49(3-4), 181-189.

Tryggvason, E., 1968. Measurement of surface deformation in Iceland by precision leveling. *Journal of Geophysical Research*, 73(22), 7039-7050.

Wendt, K., Möller, D., & Ritter, B., 1985. Geodetic measurements of surface deformations during the present rifting episode in NE Iceland. *Journal of Geophysical Research: Solid Earth*, 90(B12), 10163-10172.

Wright, T. J., Parsons, B. E., & Lu, Z., 2004. Toward mapping surface deformation in three dimensions using InSAR. *Geophysical Research Letters*, 31(1).

Zebker, H. A., & Villasenor, J., 1992. Decorrelation in interferometric radar echoes. *IEEE Transactions on geoscience and remote sensing*, 30(5), 950-959.

Zhang, H., Zeng, Q., Liu, Y., Li, X., & Gao, L., 2005. The optimum selection of common master image for series of differential SAR processing to estimate long and slow ground deformation. In *Proceedings. 2005 IEEE International Geoscience and Remote Sensing Symposium*, 2005. IGARSS'05. (Vol. 7, pp. 4586-4589). IEEE.